PATTERNED QUANTUM DOTS FOR SOLAR CELL APPLICATIONS

BY

JONATHAN D. YOUNG

THESIS

Submitted in partial fulfillment of the requirements
for the degree of Master of Science in Electrical and Computer Engineering
in the Graduate College of the
University of Illinois at Urbana-Champaign, 2011

Urbana, Illinois

Adviser:

Professor James J. Coleman

ABSTRACT

The theoretical efficiency limit of current solar cell technology, called the Shockley-Queisser limit, is about 30%. Research is underway to overcome this limit using new types of nano-sized solar cells. Quantum dots offer the potential to increase the efficiency of solar cells through carrier multiplication. In this thesis, the theory behind carrier multiplication is discussed along with the fabrication and photoluminescence characterization of patterned quantum dots.

ACKNOWLEDGMENTS

I first thank my adviser, Professor Jim Coleman for bringing me to the University of Illinois and giving me the opportunity to work in his group. His scientific expertise and guidance made this work possible. I would also like to thank my lab mates Neville Dias, Uttam Reddy, and Akash Garg for making work a fun place. I would also like to thank Tonia Siuts for helping the group to remain sane and providing help at the drop of a hat. I would also like to thank my family, most especially my amazing wife Mary.

TABLE OF CONTENTS

CHAPTER 1 – SOLAR CELL PHYSICS 1
1.1 Brief History of Solar Cells 1
1.2 Photovoltaic Generations 2
1.3 The Solar Spectrum 3
1.4 The Homojunction Solar Cell 4
1.5 Solar Cell Efficiency 6
1.6 Third Generation Photovoltaics 8
1.7 Alternative Third Generation Solar Cell Designs 11

CHAPTER 2 – QUANTUM DOT FABRICATION 13
2.1 Physics of Quantum Dots 13
2.2 Self-Assembled Quantum Dots 14
2.3 Selective Area Epitaxy of Quantum Dots 16
2.4 Wet-Etched Quantum Dot Fabrication 18

CHAPTER 3 – PHOTOLUMINESCENCE TESTING 24
3.1 Photoluminescence Spectroscopy Theory 24
3.2 Experimental Setup 25
3.3 Testing 26

REFERENCES 28

CHAPTER 1: SOLAR CELL PHYSICS

Increasing energy costs and global climate change have motivated interest in renewable resources. Wind, solar and hydroelectric are among the most common sources of renewable energy investigated today. This chapter will focus on the solar cell. The history of the solar cell will be summarized, dividing the technology into three generations. The physics behind the solar source, the photovoltaic cell and operational efficiency will be described. Finally the operating principles of third generation photovoltaics will be addressed in detail.

1.1 Brief History of Solar Cells

In 1883 Charles Fritts created the first working solar cell by melting selenium into a thin sheet on a metal substrate. He pressed a gold leaf film on top of the selenium film to be used as the top contact [1]. Nearly 60 years later, Russel Ohl, investigating the use of silicon for point contact rectifiers, noticed the material "was sensitive to visible light, generating an electromotive force independently of any applied voltage [2]." After considerable refinement, he patented his "Photo-Electromotive Force Device," a melt-grown junction solar cell [2]. Just six years later, at Bell Labs, researchers using a silicon pn junction observed six percent conversion efficiency under solar irradiance [3]. The device was termed the Bell Solar Battery [4]. Unfortunately, neither Bell Labs nor the US government saw any application for the device until 1957 when the Soviets launched Sputnik, a satellite powered completely by solar cells [5].

Motivated by the need for space power, researchers steadily improved the efficiency of the solar cell. However, it remained a technical novelty limited to space applications until the oil crisis of the 1970s. The modern infrastructure of the western world was, and still is, heavily dependent on oil. As oil shortages became a reality, governments began to look to alternative sources to supplement energy supplies, ushering in the modern era of the solar cell.

1.2 Photovoltaic Generations

Experts in the field of photovoltaics have divided solar cell technology into three generations delimited by their respective manufacturing cost per area and operating efficiency as can be seen in figure 1.1 [6].

First generation solar cells, which are single crystal Si wafer-based cells, still dominate today's market. In the laboratory, single crystal solar cells have reached efficiencies up to 25% [7], while commercially available cells have efficiencies ranging from 15% to 20% [8]. The primary cost for these cells is the Si wafer material, as the device design and fabrication are relatively simple. As long as the solar industry relies on the Si wafer, it will be forced to compete with the integrated circuit industry for the Si wafer commodity.

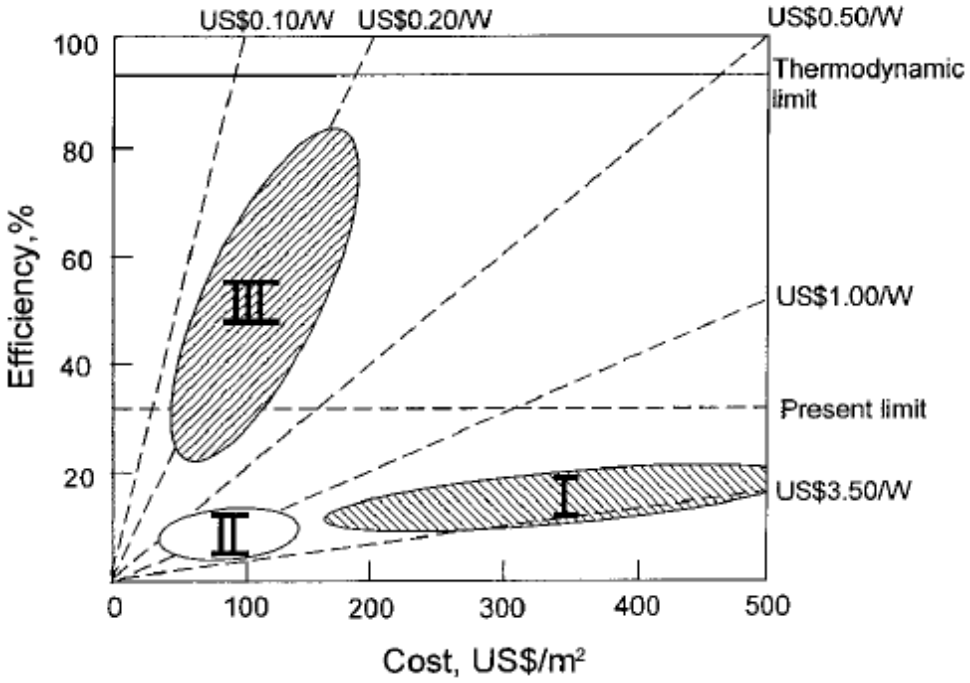

Figure 1.1: Efficiency versus cost for three solar cell generations [6]. The first, second, and third generations are labeled I, II and III respectively.

The solar cell industry is beginning to transition to second generation solar cells based on thin film technologies. Most thin film solar cells are made by depositing semiconductor material

on a glass or plastic substrate. The move away from Si substrates saves material costs, but comes at the price of decreased efficiency.

Third generation solar cells are currently in the infant stages of development. The aim of these cells is to build upon the cheaper thin film technology while improving efficiency. Several methods for improving efficiency have been proposed. In the following sections we outline the mechanisms for loss in solar cells and review cell designs aimed at minimizing these losses.

1.3 The Solar Spectrum

The sun is the earth's greatest resource. With improvements in photovoltaic technology it may too become the earth's greatest electricity source. Nuclear fusion powers the sun by creating helium from hydrogen, a process that causes the temperature to be as high as 20,000,000 K at the core and 6000 K at the surface. At these temperatures the sun emits radiation that can be approximated as a blackbody. Figure 1.2 shows a blackbody spectrum at 5670 K [9]. The extraterrestrial solar spectrum measured above earth's atmosphere is called the air mass zero (AM0) spectrum, and the solar spectrum measured on earth's surface at a latitude of 41° is called the air mass 1.5 (AM1.5) spectrum [10]. These standard spectra are used to quantify solar cell performance and are also shown in figure 1.2. Absorption and scattering losses in earth's atmosphere account for the difference in intensity and profile between the spectra.

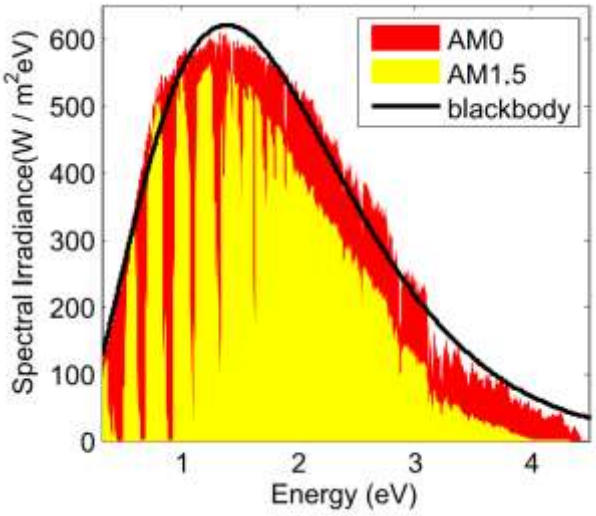

Figure 1.2: Extraterrestrial solar spectrum AM0, solar spectrum reaching earth's surface AM1.5 and spectrum of a blackbody at 5670 K.

1.4 The Homojunction Solar Cell

The single junction solar cell is the most basic example of a solar cell. It will be discussed here to outline basic solar cell operation. Figure 1.3 shows the simplified band diagram of a pn-junction with a semi-infinite absorber in the p-region. The band diagram is shown under forward bias and illumination conditions. Under forward bias and in the absence of illumination, the electron and hole populations can be derived from their respective quasi Fermi levels (dashed black line). Under illumination, photons are absorbed, creating electron-hole pairs. Despite this, there is not a significant increase in hole concentration in the p-region; however, the minority carrier electron concentration increases significantly, causing the quasi Fermi level to split (blue dashed line). Photocurrent I_L is created as free carriers diffuse to their respective contacts.

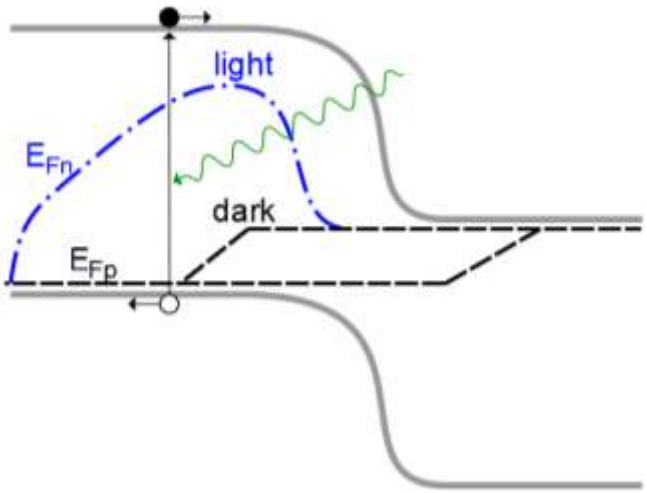

Figure 1.3: Simplified band diagram of a pn-junction solar cell. The quasi Fermi levels are depicted for dark forward-biased conditions and under illumination, in back and blue dashed lines respectively.

Figure 1.4 is a depiction of the ideal IV characteristics of the solar cell. The simple diode equation can be used to describe the current-voltage characteristics of the solar cell:

$$I = I_s\left(\exp\frac{qV}{kT} - 1\right) - I_L \tag{1.1}$$

where I_S is saturation current and I_L is photogenerated current.

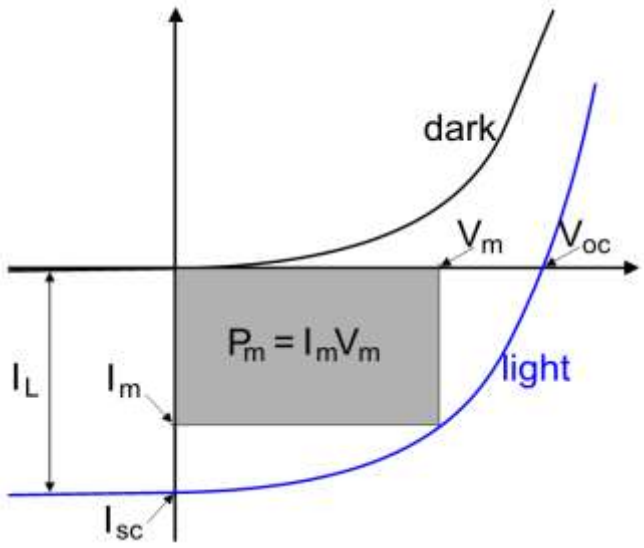

Figure 1.4: The current-voltage relationship of a homojunction solar cell, without illumination (black line) and with illumination (blue line).

The open circuit voltage V_{oc} is shown in figure 1.4 and can be derived from equation 1.1.

$$V_{oc} = \frac{kT}{q} \ln\left(\frac{I_L}{I_S} + 1\right) \tag{1.2}$$

The short-circuit current I_{SC} is also shown in the figure and is simply the photogenerated current I_L. By properly selecting a load, the maximum power P_M can be extracted; P_M is represented by the shaded region in figure 1.4 and expressed as

$$P_M = I_M V_M = F_F I_{SC} V_{OC} \tag{1.3}$$

where F_F is the fill factor. The fill factor gives a measure of the squareness of the IV curve and is defined as

$$F_F = \frac{I_M V_M}{I_{SC} V_{OC}} \tag{1.4}$$

In practice, a good value for the fill factor is 0.8. The efficiency is the ratio of the maximum power output to the incident power P_{in} and is expressed as

$$\eta = \frac{P_M}{P_{in}} \tag{1.5}$$

1.5 Solar Cell Efficiency

The most widely accepted and cited method for calculating solar cell efficiency is that described by William Shockley and Hans Queisser [11]. The purpose of this work was to provide an upper limit for the efficiency of single junction solar cells.

Shockley and Queisser make a number of assumptions to obtain their idealized limit. They start with a homojunction solar cell described above. They assume complete absorption of photons with energy above that of the band gap, resulting in the creation of exactly one electron-hole pair. Hot electrons lose all excess energy—energy above the conduction band edge—to thermalization. Infinite mobility is assumed, allowing for complete collection of generated

electron-hole pairs at the contacts. Reflection and series resistance losses are neglected. Radiative recombination losses are accounted for by treating the cell as a blackbody at a temperature of 300 °C; thus, the emitted photon areal flux density of the cell is given by

$$J_{ph}(V) = \int_{E_g}^{\infty} \frac{2\pi}{c^2 h^3} \frac{E^2}{\exp\left[\left(E - \mu_\gamma(V)\right)/kT_c\right] - 1} dE \tag{1.6}$$

where k is Boltzmann's constant, T_c is the cell temperature, and μ_γ is the chemical potential qV of the recombining electron-hole pair. The recombination current is then

$$J_0(V) = qJ_{ph}(V) \tag{1.7}$$

and the light-generated current density from the incident photon flux is

$$J_L = q\int_{E_g}^{\infty} n_{ph}(E)\, dE \tag{1.8}$$

where n_{ph} is the incident photon flux, which is approximated using a blackbody spectrum for the solar source at 6000 K. The net current density of the solar cell is then

$$J(V) = J_L - J_0(V) \tag{1.9}$$

while assuming a "detailed balance" between the incident photonic flux and the radiated flux. The power produced is given by

$$\eta = \frac{P_{out}}{P_{in}} \tag{1.10}$$

Using this process, the efficiency versus band gap can be plotted as seen in figure 1.5. Detailed balance predicts the maximum efficiency of the silicon solar cell to be 30%.

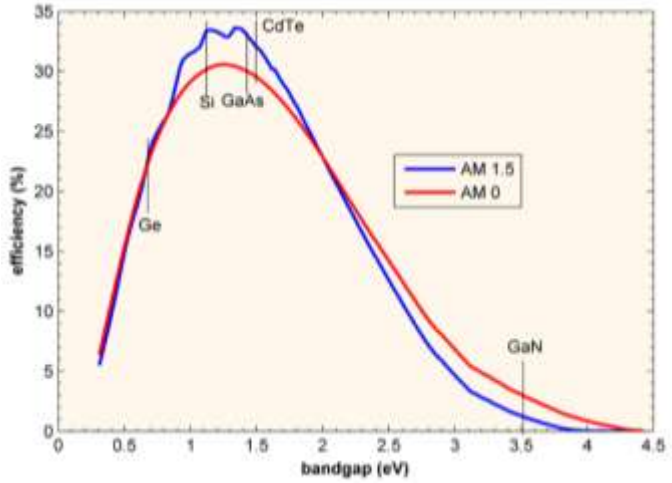

Figure 1.5: Detailed balance limit for homojunction solar cell efficiency.

History has shown this prediction to be accurate. Today the most efficient single junction Si solar cell is 25% [7]. Of course, this cell must overcome the additional losses that Shockley and Queisser neglect, and the efficiency is also recorded under the AM1.5 spectrum; these combine to account for the 5% difference from the efficiency predicted.

1.6 Third Generation Photovoltaics

The aim of third generation photovoltaics is to overcome the Shockley-Queisser efficiency limit by creating new cell designs which better utilize the solar spectrum, but with the low costs that thin film designs offer. Nearly all semiconductor-based third generation PV cells can be divided into two subcategories: intermediate band and hot carrier solar cells.

The intermediate band solar cell (IBSC) is a modified single junction solar cell with an "intermediate band" in the energy gap between the conduction and valence bands [12, 13]. The goal of this cell is to use parts of the solar spectrum below the band gap energy. Figure 1.6 shows a diagram of the band structure in an intermediate band solar cell. Photons with energy less than the gap energy can excite electrons to the intermediate band; an additional photon is used to move that electron to the conduction band.

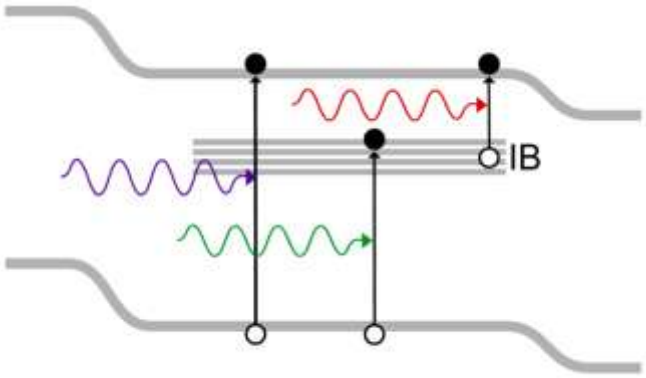

Figure 1.6: Intermediate band solar cell band diagram. The intermediate band is formed by stacking quantum dot layers.

The intermediate band (IB) cell design requires that the IB Fermi level lie within the intermediate band, allowing for a partially populated band [14, 15], and increasing the probability for electron promotion to the conduction band. To maximize efficiency, absorption should be significant in the intermediate band layers. There should also be no overlap in the absorption for transitions from valance band to intermediate band, intermediate band to conduction band and valence band to conduction band [14].

In most approaches, arrays of quantum dots are used to form the intermediate band. To improve absorption, several layers of quantum dots must be grown, a difficult process. As multiple layers of quantum dots are grown, strain builds and dislocations form, degrading the quality of the material. Thus a tradeoff between strain and absorption must be achieved. One experimental study showed that increasing the number of quantum dot layers from 10 to 20 to 50 layers actually decreased the cell performance [16].

Hot carrier solar cells are designed to take advantage of the blue end of the solar spectrum. The idea behind hot carrier solar cells is rather simple. When a photon from the blue end of the spectrum is absorbed, an energetic exciton is created. In typical cells, i.e. first and second generation solar cells, this high energy exciton loses energy as its constituents thermalize

to the band edge, losing energy to the lattice and the electron gas. In a hot carrier cell this excess energy is used by either quickly capturing the high energy electron at the contact before thermalization occurs (picosecond time scale in bulk semiconductors) or by using the excess energy to create an additional exciton, commonly referred to as multiple exciton generation.

Recently, hot carrier collection was achieved in ultra thin amorphous silicon solar cells. Kempa et al. observed an increase open circuit voltage with increasing photon energy [17]. The principal behind their design is to collect the hot carriers before thermalization has sufficient time to occur. To this end, they fabricated a p-i-n junction solar cell, an ultra thin absorber, by depositing amorphous silicon on indium tin oxide, a transparent substrate. The n and p region thicknesses were 5 nm each. The intrinsic absorber region thicknesses were varied from 10 nm to 300 nm. The cell was illuminated separately with two different frequency sources and the IV characteristics were measured. The measured open circuit voltage was greater for the higher wavelength source.

In multiple exciton generation two carriers are created for the price of one. This process is referred to as carrier multiplication in bulk material systems, while multiple exciton generation is typically used to describe this process in quantized systems. Carrier multiplication was first theorized in 1947 by S. J. Vavilov [18]; however, an experimental description for its method was not given until 1993 when Kolodinski et al. presented evidence supporting the impact ionization theory as the mechanism for carrier multiplication [19]. To visualize this process, Kolodinski showed impact ionization along the (100) direction in Si (figure 1.7). A photon is absorbed, promoting electron e1 to the conduction band. The electron e1 then relaxes to the conduction band minimum, transferring energy and momentum to e2. Energy and momentum are conserved as the vectors add vertically (energy) and horizontally (momentum) to zero. Because this process

requires three particles, it has also been described as the inverse Auger process or Auger generation.

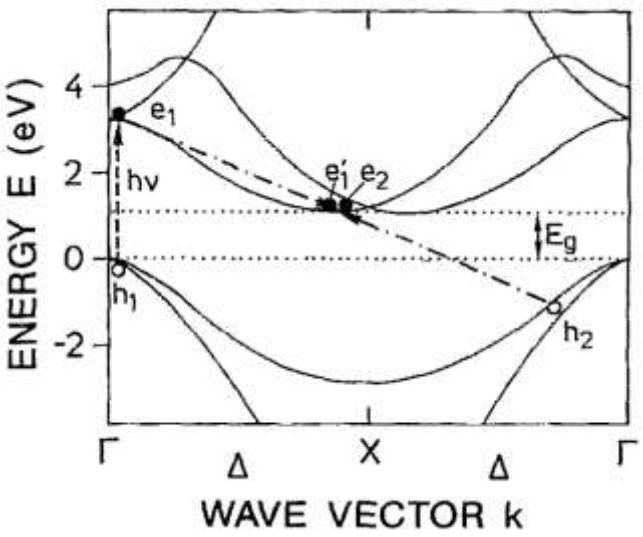

Figure 1.7: Impact ionization along the (100) direction of Si [19].

This inverse Auger process will only occur if the photon has energy at least twice that of the band gap. Multiple excitation generation has also been observed in colloidal quantum dots [20, 21]. In quantum dots, the momentum conservation requirement is relaxed as the electron is wholly confined to the quantum dot. Several solar cell designs employing colloidal quantum dots are being explored [20, 22-24]. The primary challenge for use of colloidal dots is the extraction of charge carriers. This process is also time sensitive as it must compete with the Auger recombination process [25].

1.7 Alternative Third Generation Solar Cell Designs

Many of the above mentioned third generation solar cell designs may be realized by using a different type of nanostructure: the wet-etched quantum dots. The intermediate band could be realized using three dimensional arrays of wet-etched quantum dots, which do not have the same

strain limitations inherent to self-assembled quantum dots. Hot carrier effects may also be observable in the wet-etched quantum dot. The second chapter of this thesis will describe quantum dots in greater detail; three fabrication methods will be outlined with the primary focus being the fabrication of wet-etched quantum dots.

CHAPTER 2: QUANTUM DOT FABRICATION

This chapter describes three different techniques used to fabricate quantum dots, beginning with the basic physics of quantum dots and their corresponding band structure. The traditional method for fabricating quantum dots is described. Two other fabrication techniques, selective area epitaxy of quantum dots and wet-etched quantum dots, are then outlined with the primary focus given to wet-etched quantum dots.

2.1 Physics of Quantum Dots

Bulk semiconductors are characterized by a continuous distribution of electron energy states as seen in figure 2.1(a). If one degree of quantization is added, the result is a two dimensional slab of semiconductor material, figure 2.1(b). This added quantization alters the density of states from a parabolic function to a step function. An additional degree of quantization transforms the material into a one dimensional quantum wire. Again the quantization further restricts the density of states. Three dimensional quantization leads to a zero dimensional quantum dot. The quantum dot energy spectrum is characterized by Dirac delta functions. These discrete atom-like energy states lend themselves to several useful applications including semiconductor lasers [26-28], quantum computing [29, 30], fluorescent tags for cellular imaging [31], light emitting diodes [32-34] and solar cells [12, 13, 16, 35].

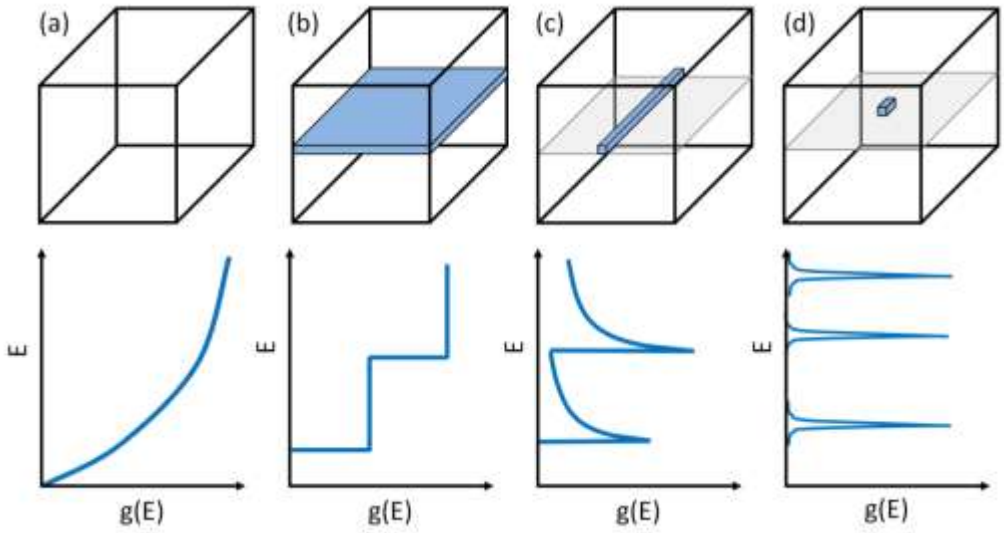

Figure 2.1: (a) Bulk material with a parabolic band diagram. (b) Quantum well with step-function band diagram. (c) Quantum wire with spike like band diagram. (d) Quantum dot with delta-function band diagram.

2.2 Self-Assembled Quantum Dots

The vast majority of quantum dots employed in semiconductor structures are self-assembled quantum dots. These dots are grown using the Stranski-Krastanov growth technique [36], in which a lightly lattice-mismatched material is epitaxially grown on a suitable substrate by molecular beam epitaxy (MBE) or metalorganic chemical vapor deposition (MOCVD). As monolayers are grown, the lattice-mismatch causes strain energy to build. Layer by layer growth continues until, at a certain critical thickness [37], strain forces the epitaxial material to coalesce into quantum dots. The critical thickness is usually on the order of several monolayers [38]. After this point, three dimensional quantum dot growth occurs. Figure 2.2 is an AFM of self-assembled quantum dots; it is evident that these dots nucleate in random positions and have a broad size distribution. These quantum dots have high densities, on the order of $1x10^{10}$ cm^{-2} to $1x10^{11}$ cm^{-2} [37, 39, 40].

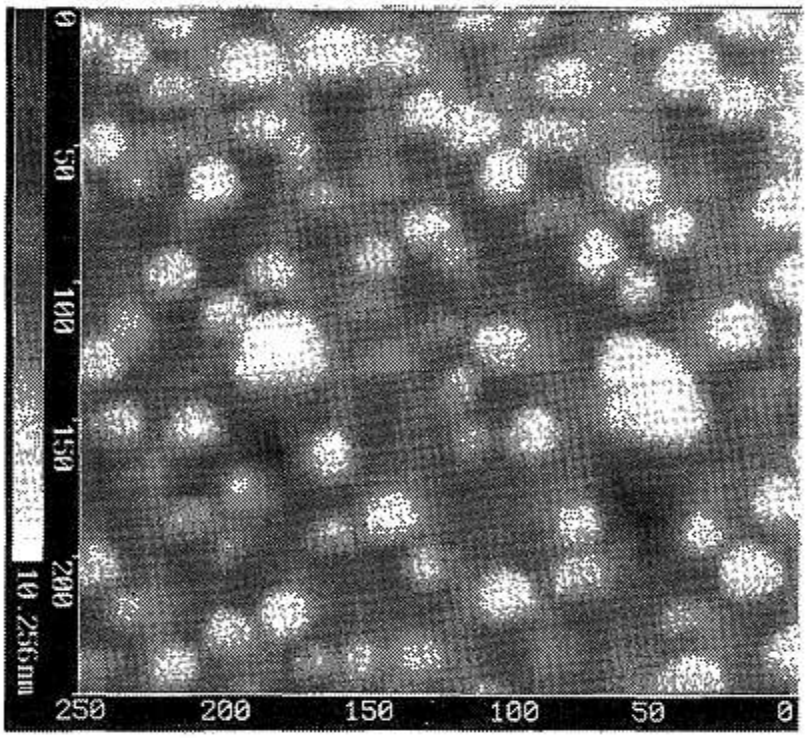

Figure 2.2: Atomic force micrograph image of self-assembled InAs quantum dots of GaAs [40].

Nonuniformity of quantum dot size can be observed experimentally in the broadening of the photoluminescence emission spectra. This inhomogeneous broadening limits the span of applications for these quantum dots, especially when strict placement of dots is required. To remedy this, alternative methods for fabricating *patterned* quantum dots have been developed. These fabrication methods can be divided into two separate subcategories: a bottom-up and a top-down approach. In the bottom-up approach a substrate or partially grown structure is patterned prior to active layer growth. The quantum dot active layer is then grown in the holes or unmasked areas. This bottom-up method is shown visually in figure 2.3(a)-(b). In the top-down approach the quantum well active layers are grown first, and then lithography and etching are used to pattern the well material into arrays of cylinders as seen in figure 2.3(c)-(d). Both of these techniques will be discussed below; a brief description of selective area epitaxy of quantum

dots will be given, followed by the primary focus of the chapter, wet chemical etching of quantum dots.

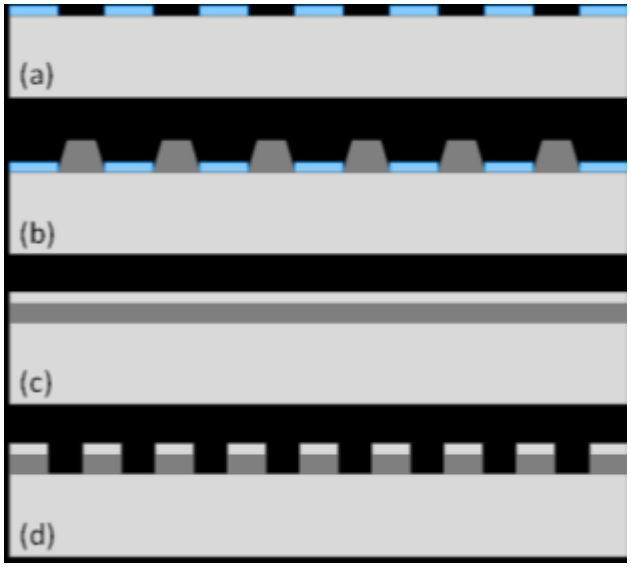

Figure 2.3: Two patterned quantum dot fabrication methods. The bottom-up approach (a)-(b) and the top-down approach (c)-(d).

2.3 Selective Area Epitaxy of Quantum Dots

Selective area epitaxy (SAE) is a growth technique used to explicitly control areas where epitaxial re-growth can occur. In this technique, a dielectric film is deposited and then patterned on the substrate. Epitaxial re-growth is then performed on the sample by metalorganic chemical vapor deposition (MOCVD) [41, 42] or molecular beam epitaxy (MBE) [43, 44]. Growth is inhibited in regions of the sample covered by the dielectric film; thus growth occurs only in unmasked areas. The mask is typically referred to as a growth inhibition mask. In MOCVD selective growth, growth precursors from the masked areas diffuse to the exposed areas. Diffusion increases the concentration of precursors near the masked areas resulting in an increase in the semiconductor growth rate in that area. This effect is called growth enhancement [45, 46]. Ternary and quaternary alloys also experience a composition shift in these areas due to the different diffusion coefficients of precursor materials [47]. A schematic view of growth

enhancement is given in figure 2.4. A sample with a growth inhibition mask before and after selective growth is shown. Growth enhancement of the well layer occurs near oxide stripes. If the sizes are much smaller than the diffusion coefficients (center stripe opening in figure 2.4), the growth rate is relatively uniform.

Figure 2.4: A cross section SiO_2 growth inhibition mask on a GaAs substrate before (a) and after (b) after selective growth of InGaAs layer.

Elarde et al. were the first to report patterned quantum dots with explicitly defined position grown by selective area epitaxy [48]. To fabricate these dots, a SiO_2 growth inhibition mask was fabricated on the substrate by first depositing a layer of SiO_2 on the substrate. The standard optical lithography and wet etching are then used to define the overall shape of the growth inhibition mask, be it square oxide areas for photoluminescence testing or oxide stripes for use in a laser structure. Electron-beam lithography and a BHF etch are used to pattern an array of holes in the mask. The dot layer is then selectively grown in the unmasked holes. After the dot layer growth, the growth inhibition mask is removed and the upper dot barrier is grown. This method of patterned dot growth can be severely hampered by growth enhancement and composition enhancement effects if the overall mask geometry is on the diffusion length of the growth precursors.

2.4 Wet-Etched Quantum Dot Fabrication

To overcome the limitations of SAE quantum dots, the top-down technique for the patterning of quantum dots was adopted. In this group, the technique was first reported by Verma and Coleman [49]; it has also been reported elsewhere by Hirayama et al. in 1994 [50]. In this technique, the quantum dot material is grown first, thus rigidly enforcing the dot material composition. Lithography and wet-etching are then used to pattern the quantum well into arrays of quantum dots.

The technique reported in this thesis is a variant of those developed by Verma, who used two separate techniques to fabricate the quantum dot etch mask. In the first technique a SiO_2 etch mask was formed via development of HSQ, a positive electron-beam resist. In the second method, titanium was evaporated onto the developed PMMA, a negative electron-beam resist, and lifted off to reverse the pattern that serves as the wet etch mask. In the latter technique, liftoff causes fracturing of the titanium resulting in less uniform dots. To address this problem, the new technique reported in this thesis was developed.

Base structure growth

The wet-etched dots described in this section were incorporated into a base structure that has been optimized for photoluminescence measurements. The base structure growth was performed in an atmospheric pressure MOCVD reactor. It consists of a 100 nm GaAs n+ buffer layer grown on an n+ (100) GaAs wafer followed by the growth of a 1 μm n-type $Al_{0.75}Ga_{0.25}As$ layer and a 100 nm undoped GaAs lower barrier. The AlGaAs layer is used to help confine the electrons and holes to the vicinity of the quantum dot layer. Immediately after the GaAs lower barrier, a 86.9 Å $In_{0.31}Ga_{0.69}As$ quantum well is grown and capped with a 4 nm GaAs layer.

Alignment target fabrication

Once the base structure and quantum well growth are complete, alignment targets are fabricated. Plasma enhanced chemical vapor deposition (PECVD) is used to deposit 30 nm of SiO_2. The sample is spin coated at 3000 RPM with AZ-5214E photoresist. Negative optical lithography and development in AZ-327 are used to open up the alignment target patterns in the photoresist. 100 Å of Ti and 1500 Å of Au are evaporated onto the sample. The titanium layer is used to promote adhesion of the gold layer to the underlying SiO_2. The sample is left in acetone for 2 hours to lift off the metal layer leaving gold alignment targets. The sample is then rinsed in methanol and isopropyl alcohol (IPA). Sonication is not used to speed the process because it would cause fracturing of the gold, making subsequent registration of the sample in the electron beam lithography tool extremely difficult or even impossible. The sample is then cleaned in an oxygen plasma for 3 minutes with an incident power of 100 W. The gold alignment targets are encapsulated with 50 nm of SiO_2 deposited by PECVD. This oxide layer is also used to create the etch mask for pattern transfer into the well layer.

Etch mask fabrication

The electron beam resist of 2% polymethylmethacrylate (PMMA) in anisole is spin coated on the sample at 4000 RPM. Direct write electron beam lithography is used to write 18 square mesh patterns. Figure 2.5 is a schematic of the arrangement of the 18 square mesh patterns. Three rows of mesh pattern are written; in each row there are 6 mesh patterns with the same pitch. The pitches scale from top to bottom 125 nm, 150 nm and 200 nm respectively. The electron beam is varied from square to square, increasing from left to right.

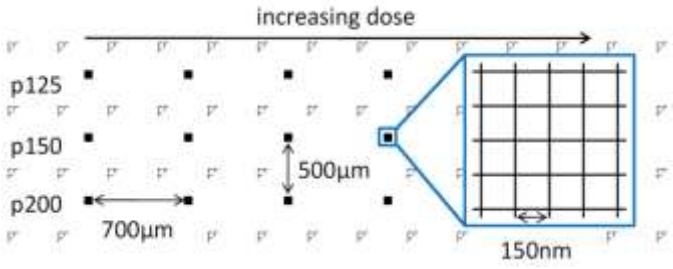

Figure 2.5: Arrangement of mesh patterns.

Following exposure, the sample is developed in a solution of 1:2 *methyl isobutyl ketone* (*MIBK*) to isopropyl alcohol for 3 minutes at 10 °C. After development the sample is rinsed for 30 seconds in IPA. Three different square grid patterns are written; lines with 200 nm spacing, 150 nm spacing and 125 nm spacing result in dot densities of 2.5×10^9, 4.4×10^9 and 6.4×10^9 respectively. Figure 2.6 is an SEM image of the developed PMMA pattern for the 200 nm spaced grid. The dark squares are the remaining PMMA, the lighter lines are the underlying oxide.

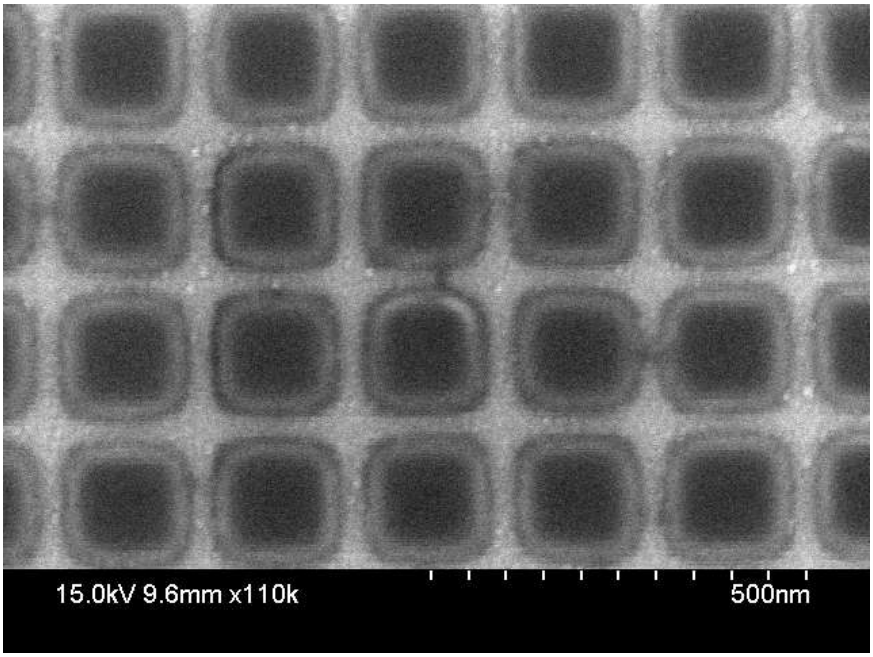

Figure 2.6: SEM image of developed PMMA grid pattern with line spacing of 200 nm.

The pattern is transferred to the underlying oxide with Freon reactive ion etch (RIE). The oxide is etched approximately 30 nm deep, leaving 20 nm of unetched oxide. The PMMA is stripped by sonicating the sample in acetone, methanol and IPA, each for 2 minutes. An oxygen descum is then performed to remove any remaining PMMA. Complete removal of PMMA is essential; when exposed to BHF, PMMA creates a residue that is extremely difficult to remove.

The oxide is then etched in a dilute BHF solution, 1:50 HF to NH_4F, to open up the oxide grid to the underling GaAs. The resulting rounded oxide squares serve as the wet-etch mask for the quantum dots. In this situation dry etching is combined with wet etching to minimize damage to the underlying quantum well. A dry etch is better suited for preserving mask feature sizes; however, any dry etch exposure causes defects in the underlying quantum well.

Quantum dot etching and barrier regrowth

To transfer the mask pattern to the quantum well, we use a solution of 1:4:495 phosphoric acid to hydrogen peroxide to deionized water. The solution is diluted to keep the etch rate manageable and results reproducible. After the pattern is etched through the well layer, the oxide is stripped in BHF leaving circular disks of well material or quantum dots. An SEM of the three different dot patterns is given in figure 2.7 (a)-(c).

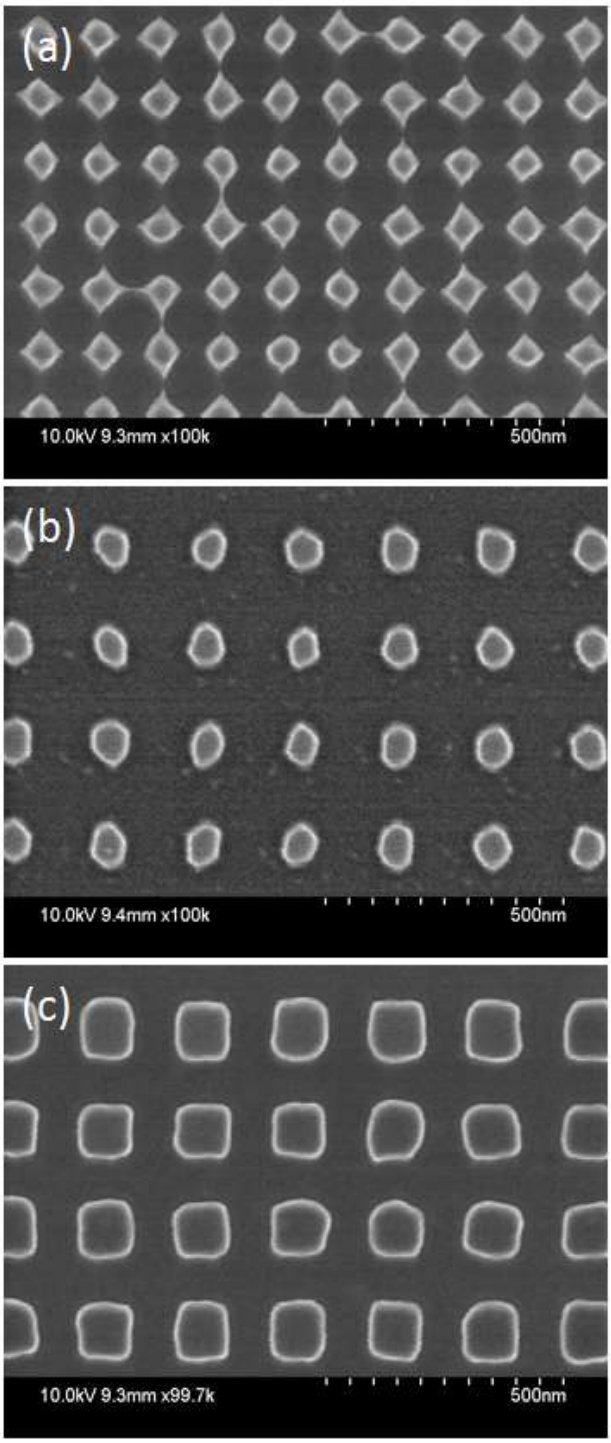

Figure 2.7: SEM image of patterned quantum dots on a pitch of (a) 125 nm, (b) 150 nm and (c) 200 nm.

Native oxide is removed in a nitrogen environment and the sample is transferred to an AIX 200/4 MOCVD reactor for regrowth. Complete removal of the native oxide is critical for the quality of this quantum dot layer. Regrowth of the GaAs barrier and upper core layer is performed at 100 mbar at 625 °C in a reactor at a slow growth rate of 0.2 nm/s. The slow growth rate is used again to promote quality of the dot layer. A 100 nm $Al_{0.75}Ga_{0.25}As$ layer and a GaAs layer are also grown. The low growth temperature of 625 °C is used to prevent indium diffusion from the dots layer. The AlGaAs layer is used to help confine the quantum dots to the vicinity of the dot layer, and the GaAs layer is used to prevent oxidation of the AlGaAs.

The final steps are used to prepare the sample for photoluminescence testing. The sample is coated with gold, and square apertures are opened directly above the dot pattern. These apertures prevent photoexcitation in regions of the sample not covered by dots. Lithography is first performed to mask the dot regions and for liftoff. The sample is spin coated at 3000 RPM with AZ-5214E. Optical lithography and development in AZ-327 are used to create the pattern. The metal layers are then evaporated, first 100 Å of Ti for adhesion and then 500 Å of Ag. As described earlier, liftoff is performed in acetone for two hours. The sample is then rinsed in methanol and IPA.

CHAPTER 3: PHOTOLUMINESCENCE TESTING

This chapter describes photoluminescence theory and details the particular apparatus used while providing important considerations that must be addressed. Finally, preliminary photoluminescence spectra are presented.

3.1 Photoluminescence Spectroscopy Theory

Photoluminescence is a measurement technique in which a sample is excited via an optical source and luminescence spectra are collected. It can be used to determine material properties such as location and concentrations of defects or other nonradiative recombination centers as well as surface and interface quality. The electronic structure can also be inferred by studying radiative recombination spectra or luminescence and relating spectral wavelength and intensity to electronic states and transition probabilities (figure 3.1), as well as to populations and lifetimes of the state. Both electron and hole concentrations control luminescence intensity, and in bipolar systems [51] transitions to both hole subbands should be accounted for.

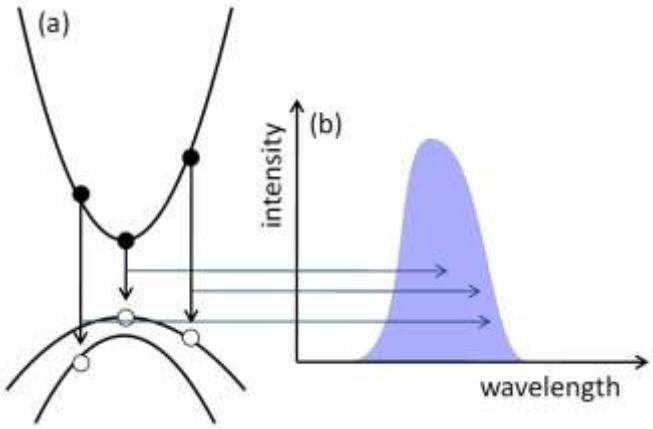

Figure 3.1: (a) Band diagram of a direct-gap semiconductor. (b) Luminescence spectra corresponding to radiative transitions in (a).

In quantized systems where carriers are tightly confined, the electric field dependent subband population dynamics of carriers should also be considered. By studying the temporal dependence of luminescence spectra (time-resolved photoluminescence) further insight can be gained regarding carrier lifetimes, transition probabilities and thermalization rates. In these experiments the optical source, wavelength and intensity are chosen specifically to probe particular electronic states. An extension of time-resolved photoluminescence spectroscopy is pump probe spectroscopy. The probe source is added and used to "probe" a particular electronic state or transition. Pump probe spectroscopy was used by Schaller and Klimov to detect multiple exciton generation in colloidal quantum dots [21] and is still the only means whereby multiple exciton generation is observed in quantum dots.

3.2 Experimental Setup

Photoluminescence measurements were performed using the 488 nm line of an argon-ion gas laser for sample excitation and spectra were resolved using a Spex 1-m monochromator. Refer to figure 3.2(a) for the following discussion. The excitation light is represented by the purple line and luminescence by the orange line. A confocal arrangement is used, were the objective both focuses the source light onto the dot areas and collects the dot luminescence. The cold mirror is transmissive from 700 to 1500 nm, thus allowing for luminescence transmission. The luminescence is focused on the entrance slit of the monochromator. Figure 3.2(b) shows a diagram of a Czerny-Turner type monochromator used in this experiment. The entrance slit is used to diffract the beam, and as it reaches the first parabolic mirror, the wavefronts are mostly parallel. The parabolic mirror further collimates the beam and directs it to the diffraction grating. The grating disperses the beam spectrally and directs it to the second parabolic mirror, which focuses the wavelength components roughly to the plane of the exit slit. The spectral

resolution of the monochromator is set by adjusting both the entrance and exit slits. From the monochromator, the light is absorbed by a liquid nitrogen cooled germanium detector.

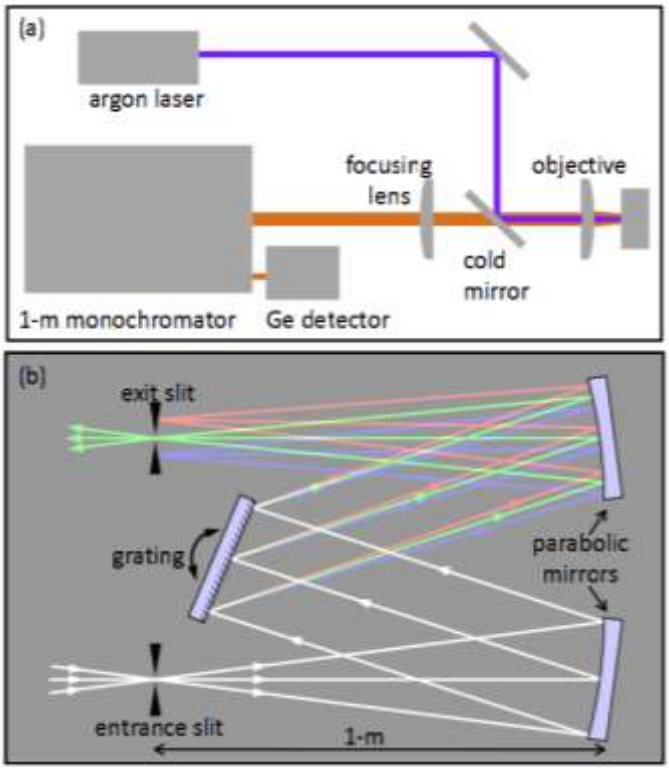

Figure 3.2: (a) Diagram of photoluminescence arrangement used. (b) Diagram of 1 m long Czerny-Turner type monochromator.

3.3 Testing

The quantum dot sample was cooled to 77 K in a liquid nitrogen cryostat. The excitation light was chopped and then roughly focused onto the sample plane with a 50x objective. The reason for focusing the light is to limit it to a single quantum dot pattern. The defocused spot is approximately 100 μm in diameter; the light is isolated from the surrounding GaAs layers by the metal aperture mask described in the previous chapter. The intensity of the light at the sample plane was 3.2 kW/cm^2 at a wavelength of 488 nm. If every incident photon is assumed to generate one electron-hole pair, there are 2.5x10^{18} pairs generated per second. We were forced

to use such high intensities to obtain any appreciable luminescence signal at the detector. The quantum dot patterns were tested against the quantum well on unetched regions of the sample.

Figure 3.3 shows the best obtained photoluminescence spectra for the three different quantum dot pitch patterns and a control quantum well. All spectra are normalized to the quantum well spectra. The quantum dot spectra are blue shifted by 80 nm, 44 nm and 22 nm. Figure 3.3 shows the spectra of three quantum dot patterns, all on a 200 nm pitch with increasing dose levels for the e-beam write. As described in the previous chapter, an increased dose level will result in smaller diameter quantum dots.

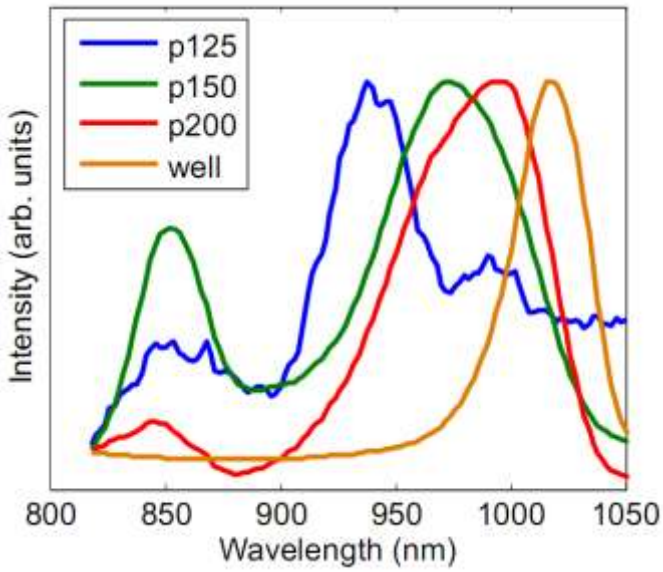

Figure 3.3: Luminescence spectra obtained from three different quantum dot pitch patterns, each normalized to the quantum well.

Unfortunately the photoluminescence spectra for these dot samples tend to change from run to run. We also believe that the intensity of the pump light was heating the sample in the vicinity of the dots; this high intensity was also dramatically altering the carrier population levels, so much so that we cannot comfortably report significant results from these spectra. For these reasons we are required to repeat these measurements in a different photoluminescence setup better suited for measurement of micron sized areas.

REFERENCES

[1] C. E. Fritts, "On a new form of selenium photocell," *Proc. Am. Assoc. Adv. Sci.,* vol. 33, p. 97, 1883.

[2] R. S. Ohl, "Light-sensitive electric device including silicon," U. S. Patent 2,443,542, June 27, 1941.

[3] D. M. Chapin, C. S. Fuller, and G. L. Pearson, "A new silicon p-n junction photocell for converting solar radiation into electrical power," *J. Appl. Phys.,* vol. 25, pp. 676-677, June 1954.

[4] M. B. Prince, "Silicon solar energy converters," *J. Appl. Phys.,* vol. 26, pp. 534-540, May 1955.

[5] H. J. Queisser, "Detailed balance limit for solar cell efficiency," in *EMRS 2008 Spring Conference Symposium K: Advanced Silicon Materials Research for Electronic and Photovoltaic Applications*, vol. 159-160, 2009, pp. 322-328.

[6] M. A. Green, "Third generation photovoltaics: Ultra high conversion efficiency at low cost," *Prog. Photovolt. Res. Appl.,* vol. 9, pp. 123-135, March 2001.

[7] M. A. Green, "The path to 25% silicon solar cell efficiency: History of silicon cell evolution," *Prog. Photovolt. Res. Appl.,* vol. 17, p. 183, May 2009.

[8] M. A. Green, K. Emery, Y. Hishikawa, and W. Warta, "Solar cell efficiency tables (version 34)," *Prog. Photovolt. Res. Appl.,* vol. 17, pp. 320-326, August 2009.

[9] J. E. Parrott, "Choice of an equivalent black body solar temperature," *Sol. Energy,* vol. 51, p. 195, 1993.

[10] C. Riordan and R. Hulstrom, "What is an air mass 1.5 spectrum?" in *Conference Record of the Twenty First IEEE Photovoltaic Specialists Conference – 1990,* vol. 2, 1990, p. 1085.

[11] W. Shockley and H. J. Queisser, "Detailed balance limit of efficiency of p-n junction solar cells," *J. Appl. Phys.,* vol. 32, pp. 510-519, 1961.

[12] A. Luque and A. Marti, "Increasing the efficiency of ideal solar cells by photon induced transitions at intermediate levels," *Phys. Rev. Lett.,* vol. 78, p. 5014, June 30, 1997.

[13] A. Marti, L. Cuadra, and A. Luque, "Quantum dot intermediate band solar cell," in *Conference Record of the Twenty-Eighth IEEE Photovoltaic Specialists Conference, 2000,* 2000, pp. 940-943.

[14] A. Marti, L. Cuadra, and A. Luque, "Partial filling of a quantum dot intermediate band for solar cells," *IEEE Trans. Electron Devices,* vol. 48, p. 2394, October 2001.

[15] A. Luque, A. Marti, N. Lopez, E. Antolin, E. Canovas, C. Stanley, C. Farmer, L. J. Caballero, L. Cuadra, and J. L. Balenzategui, "Experimental analysis of the quasi-Fermi level split in quantum dot intermediate-band solar cells," *Appl. Phys. Lett.,* vol. 87, p. 083505, August 22, 2005.

[16] N. Lopez, A. Marti, A. Luque, C. Stanley, C. Farmer, and P. Diaz, "Experimental analysis of the operation of quantum dot intermediate band solar cells," *J. Sol. Energy Eng.,* vol. 129, pp. 319-322, August 2007.

[17] K. Kempa, M. J. Naughton, Z. F. Ren, A. Herczynski, T. Kirkpatrick, J. Rybczynski, and Y. Gao, "Hot electron effect in nanoscopically thin photovoltaic junctions," *Appl. Phys. Lett.,* vol. 95, p. 233121, 2009.

[18] S. J. Vavilov, "The duration of luminescence," *A. S. USSR,* vol. 3, p. 293, 1952.

[19] S. Kolodinski, J. H. Werner, T. Wittchen, and H. J. Queisser, "Quantum efficiencies exceeding unity due to impact ionization in silicon solar cells," *Appl. Phys. Lett.,* vol. 63, p. 2405, October 25, 1993.

[20] A. J. Nozik, "Quantum dot solar cells," *Phys. E-Low-Dimens. Syst. Nanostruct.,* vol. 14, pp. 115-120, April 2002.

[21] R. D. Schaller and V. I. Klimov, "High efficiency carrier multiplication in PbSe nanocrystals: implications for solar energy conversion," *Phys. Rev. Lett.,* vol. 92, p. 186601, May 7, 2004.

[22] R. Plass, S. Pelet, J. Krueger, M. Gratzel, and U. Bach, "Quantum dot sensitization of organic-inorganic hybrid solar cells," *J. Phys. Chem. B,* vol. 106, pp. 7578-7580, August 2002.

[23] S. A. McDonald, G. Konstantatos, S. G. Zhang, P. W. Cyr, E. J. D. Klem, L. Levina, and E. H. Sargent, "Solution-processed PbS quantum dot infrared photodetectors and photovoltaics," *Nature Mater.,* vol. 4, p. 138, February 2005.

[24] I. Robel, V. Subramanian, M. Kuno, and P. V. Kamat, "Quantum dot solar cells. Harvesting light energy with CdSe nanocrystals molecularly linked to mesoscopic TiO2 films," *J. Am. Chem. Soc.,* vol. 128, pp. 2385-2393, February 2006.

[25] V. I. Klimov, "Optical nonlinearities and ultrafast carrier dynamics in semiconductor nanocrystals," *J. Phys. Chem. B,* vol. 104, pp. 6112-6123, July 6, 2000.

[26] X. Huang, A. Stintz, C. P. Hains, G. T. Liu, J. Cheng, and K. J. Malloy, "Efficient high-temperature CW lasing operation of oxide-confined long-wavelength InAs quantum dot lasers," *Electron. Lett.,* vol. 36, pp. 41-42, January 2000.

[27] I. R. Sellers, H. Y. Liu, K. M. Groom, D. T. Childs, D. Robbins, T. J. Badcock, M. Hopkinson, D. J. Mowbray, and A. S. Skolnick, "1.3 μm InAs/GaAs multilayer quantum-dot laser with extremely low room-temperature threshold current density," *Electron. Lett.,* vol. 40, pp. 1412-1413, October 2004.

[28] S. Fathpour, Z. Mi, and P. Bhattacharya, "High-speed quantum dot lasers," *J. Phys. D (Appl. Phys.),* vol. 38, pp. 2103-2111, July 7, 2005.

[29] R. B. Patel, A. J. Bennett, K. Cooper, P. Atkinson, C. A. Nicoll, D. A. Ritchie, and A. J. Shields, "Quantum interference of electrically generated single photons from a quantum dot," *Nanotechnol.,* vol. 21, p. 274011, July 2009.

[30] C. S. Lent and P. D. Tougaw, "A device architecture for computing with quantum dots," *Proc. of the IEEE,* vol. 85, pp. 541-557, April 1997.

[31] X. Michalet, F. F. Pinaud, L. A. Bentolila, J. M. Tsay, S. Doose, J. J. Li, G. Sundaresan, A. M. Wu, S. S. Gambhir, and S. Weiss, "Quantum dots for live cells, in vivo imaging, and diagnostics," *Science,* vol. 307, pp. 538-544, January 28, 2005.

[32] S. Coe, W. Wing-Keung, M. Bawendi, and V. Bulovic, "Electroluminescence from single monolayers of nanocrystals in molecular organic devices," *Nature,* vol. 420, pp. 800-803, December 26, 2002.

[33] S. Chaudhary, M. Ozkan, and W. C. W. Chan, "Trilayer hybrid polymer-quantum dot light-emitting diodes," *Appl. Phys. Lett.,* vol. 84, pp. 2925-2927, April 12, 2004.

[34] H. P. D. Yang, Y. Zao-En, G. Lin, K. Hao-Chung, and J. Y. Chi, "InGaAs submonolayer quantum-dot photonic-crystal LEDs for fiber-optic communications," *Microelectron. Reliab.,* vol. 50, pp. 688-691, May 2010.

[35] A. J. Nozik, "Exciton multiplication and relaxation dynamics in quantum dots: Applications to ultrahigh-efficiency solar photon Conversion," *Inorg. Chem.,* vol. 44, p. 6893, October 1, 2005.

[36] E. Bauer, "Phaenomenologische Theorie der Kristallabscheidung an Oberflaechen I," *Zeitschrift för Kristallographie,* vol. 110, pp. 372-394, 1958.

[37] D. Leonard, K. Pond, and P. M. Petroff, "Critical layer thickness for self-assembled InAs islands on GaAs," *Phys. Rev. B,* vol. 50, p. 11687, 1994.

[38] T. S. Yeoh, C. P. Liu, R. B. Swint, A. E. Huber, S. D. Roh, C. Y. Woo, K. E. Lee, and J. J. Coleman, "Epitaxy of InAs quantum dots on self-organized two-dimensional InAs islands by atmospheric pressure metalorganic chemical vapor deposition," *Appl. Phys. Lett.,* vol. 79, p. 221, July 2001.

[39] B. Daudin, F. Widmann, G. Feuillet, Y. Samson, M. Arlery, and J. L. Rouviere, "Stranski-Krastanov growth mode during the molecular beam epitaxy of highly strained GaN," *Phys. Rev. B,* vol. 56, pp. 7069-7072, 1997.

[40] Y. Sugiyama, Y. Nakata, K. Imamura, S. Muto, and N. Yokoyama, "Stacked InAs self-assembled quantum dots on (001)GaAs grown by molecular beam epitaxy," *Jpn. J. Appl. Phys.,* vol. 35, pp. 1320-1324, February 1996.

[41] T. M. Cockerill, D. V. Forbes, H. Han, B. A. Turkot, J. A. Dantzig, I. M. Robertson, and J. J. Coleman, "Wavelength tuning in strained layer InGaAs-GaAs-AlGaAs quantum well lasers by selective-area MOCVD," *J. Electron. Mater.,* vol. 23, pp. 115-119, 1994.

[42] K. Kumakura, K. Nakakoshi, M. Kishida, J. Motohisa, T. Fukui, and H. Hasegawa, "Dynamics of selective metalorganic vapor phase epitaxy growth for GaAs/AlGaAs micro-pyramids," *J. Cryst. Growth,* vol. 145, pp. 308-313, December 1994.

[43] L. Seung-Chang, K. J. Malloy, and S. R. J. Brueck, "Nanoscale selective growth of GaAs by molecular beam epitaxy," *J. Appl. Phys.,* vol. 90, pp. 4163-4168, October 2001.

[44] S. C. Lee, A. Stintz, and S. R. J. Brueck, "Nanoscale limited area growth of InAs islands on GaAs(001) by molecular beam epitaxy," *J. Appl. Phys.,* vol. 91, pp. 3282-3288, March 2002.

[45] M. A. Cotta, R. A. Hamm, T. W. Staley, R. D. Yadvish, L. R. Harriott, and H. Temkin, "Scanning force microscopy measurement of edge growth rate enhancement in selective area epitaxy," *Appl. Phys. Lett.,* vol. 62, pp. 496-498, 1993.

[46] Y. Mishima, N. Kaida, M. Sugiyama, Y. Shimogaki, and Y. Nakano, "Two-dimensional simulation of the growth enhancement in selective area metal-organic vapor phase epitaxy," in *Symposium on Fundamental Gas-Phase and Surface Chemistry of Vapor-Phase Materials Synthesis*, 1999, pp. 364-369.

[47] T. Fujii and M. Ekawa, "Origin of compositional modulation of InGaAs in selective-area metalorganic vapor-phase epitaxy," *J. Appl. Phys.,* vol. 78, pp. 5373-5386, November 1995.

[48] V. C. Elarde, T. S. Yeoh, R. Rangarajan, and J. J. Coleman, "Patterned InGaAs quantum dots by selective area MOCVD," in *Thirty-First International Symposium on Compound Semiconductors,* 2004, p. 353.

[49] V. B. Verma and J. J. Coleman, "High density patterned quantum dot arrays fabricated by electron beam lithography and wet chemical etching," *Appl. Phys. Lett.,* vol. 93, p. 111117, September 15, 2008.

[50] H. Hirayama, K. Matsunaga, M. Asada, and Y. Suematsu, "Lasing action of $Ga_{0.67}In_{0.33}As$/GaInAsP/InP tensile-strained quantum-box laser," *Electron. Lett.,* vol. 30, pp. 142-143, 1994.

[51] L. Schrottke, R. Hey, and H. T. Grahn, "Population properties and carrier dynamics in a GaAs/(Al,Ga)As double-quantum-well superlattice investigated by time-resolved photoluminescence spectroscopy," *Appl. Phys. Lett.,* vol. 79, pp. 629-631, July 2001.